Contents lists available at ScienceDirect

Ceramics International

In vitro biodegradability–bioactivity–biocompatibility and antibacterial properties of SrF$_2$ nanoparticles synthesized by one-pot and eco-friendly method based on ternary strontium chloride-choline chloride-water deep eutectic system

Mohammad Karimi, Saeed Hesaraki*, Nader Nezafati

Department of Nanotechnology & Advanced Materials, Materials and Energy Research Center, Karaj, Iran

ABSTRACT

Strontium fluoride (SrF$_2$) nanoparticles were synthesized using strontium chloride-choline chloride-water deep eutectic system at 80 °C. XRD, FESEM, TEM, EDS and Raman spectroscopy were employed to characterize the synthesized nanoparticles. The analytical results confirmed the synthesis of SrF$_2$ nanoparticles crystallized in the cubic crystal system with a mean crystal diameter of 26 nm, average particle size of 40 nm, Sr/F atomic ratio of 1.85 and high elemental and structural purity. The biodegradation and bioactivity of as-synthesized SrF$_2$ nanoparticles were examined in the artificial saliva (AS) and simulated body fluid (SBF). The nanoparticles showed maximum weight loss of 33% after immersion in the AS solution for 14 days. The results of SEM-EDS and Raman spectroscopy revealed the formation of a dense apatite layer on the surface of the nanoparticles after 14 days of incubation in the SBF suggesting the good *in vitro* bioactivity. Antibacterial study demonstrated the excellent antibacterial activity of SrF$_2$ nanoparticles against the *Streptococcus mutans* in such a way that ∼ 100% bacteria elimination was achieved in presence of the nanoparticles compared with control. This was attributed to the increase of pH and osmotic pressure of the environment caused by the enhanced release of Sr^{2+} and F$^-$ ions from the synthesized SrF$_2$ nanoparticles. MTT cytotoxicity assay and acridine orange (AO) staining test on the human mesenchymal stem cells (hMSCs) confirmed the biocompatibility of SrF$_2$ nanoparticles.

1. Introduction

Fluoride is an essential element for the formation and development of hard tissues, including teeth and bones. Clinical research shows that the presence of fluoride has a profound effect on the formation and resorption of bone in the body both quantitatively and quantitatively [1,2]. Fluoride has also shown an effective role in treating osteoporosis, because it could reduce the demineralization and enhance remineralization rate via improving the osteoblasts activity both *in vitro* and *in vivo*, which in turn increases bone density. Furthermore, fluoride is widely used as an anticaries agent by inhibiting the dental plaque acid production and improving the formation of acid resistant fluorapatite crystals. Accordingly, World Health Organization (WHO) has recommended the daily fluoride intake of 1.5 mg to improve the oral health and avoid dental caries [2–5].

Fluoride is also known for its antibacterial properties. In this regard, fluoride affects the bacterial metabolism in several ways. Recent reports have shown that fluoride acts as a quasi-irreversible inhibitor on the glycolytic enzyme, especially on the enolase, to interfere bacterial metabolism [4,6]. Fluoride also increases the permeability of the cell membrane to the protons and compromises the ATPases functionality in exporting protons. Accordingly, the environment acidity is increased and at the same time, the bacterial tolerance to acidic conditions is reduced resulting in inhibition of bacterial activity [1,7,8].

Nanostructured metal fluorides have shown to be a good source of fluoride because of their good solubility and high surface area [4,9]. Meanwhile, strontium fluoride (SrF$_2$) is a more interesting option especially for biomedical applications. In fact, strontium could manage dentine hypersensitivity and prevent dental caries in synergy with fluoride [2].

Various methods have been developed for the synthesis of metal fluorides especially SrF$_2$, including the thermolysis of precursors, flame pyrolysis, microemulsion and reverse micelle, hydrothermal-solvothermal synthesis, mechanochemical synthesis, coprecipitation in non-aqueous media, and sol-gel method which has been mentioned in detail in a review paper published by Fedorov et al. [10]. Despite their

well known advantages, the aforementioned methods generally face some major challenges such as strict synthesis conditions (high temperature and high pressure), the need of specific laboratory equipment and facilities, use of harmful precursors such as toxic surfactants and organic solvents with high vapor pressure, inability to recover solvents, use of expensive precursors such as alkoxide and poly-fluoride salts, time-consuming synthesis process, etc [10]. The challenges have led to the economic inefficiency as well as non-compliance with the principles of green chemistry, which nowadays is considered as a fundamental criterion for the development of synthesis methods [11].

In a study conducted by Lashgari et al., SrF_2, MgF_2 and SrF_2-MgF_2 (50:50) nanocomposites were synthesized using coprecipitation method in the presence of metal chlorides and ammonium fluoride precursors. Characterization results showed the formation of SrF_2, MgF_2 and SrF_2-MgF_2 nanoparticles with a mean diameter of 43, 24, and 35 nm, respectively. TEM micrographs revealed the synthesis of nanoparticles with spherical morphology and high degree of agglomeration in all cases. In this study, the antibacterial properties of the synthesized nanomaterials against *S. Aureus*, *B. Subtilis* and *E. Aklay* bacteria were investigated. According to the results obtained on the growth-inhibitory range around the nanomaterials, SrF_2-MgF_2 nanocomposite showed a better antibacterial performance compared to its components [12]. Du et al., succeed in synthesis of MF_2 (M = Mg, Ca, Sr) nanoparticles with uniform size distribution by thermal decomposition of the relevant trifluoroacetate precursors in high-boiling point solvents including oleic acid, oleyl amine and 1-octadecene. Using this method, MgF_2 nanoneedles with tetrahedral crystal structure and particle size of 13 nm, CaF_2 nanoplates/nanopolyhedra with cubic crystal structure and particle size of 32 nm, and SrF_2 nanoplates/nanowires with cubic crystal structure and particle size of 35 nm were synthesized [13]. Schmidt et al., synthesized SrF_2 nanoparticles by sol-gel method. Characterization of the obtained powder showed the formation of SrF_2 nanoparticles with cubic crystal structure, crystallite size of 10 nm, average particle size of 65 nm, and specific surface area of 180 $m^2 g^{-1}$ [14]. Grass et al., synthesized BaF_2, SrF_2, and CaF_2 nanoparticles using a flame spray method. To this end, they used metal 2-ethyl hexanoate and fluorobenzoate precursors as fluoride precursors in a methane-oxygen flame. BaF_2, SrF_2 and CaF_2 products showed a cubic crystal structure and particle size generally less than 60 nm [15].

The present study aimed at synthesis and characterization of SrF_2 nanoparticles. To this purpose, using an innovative approach, ternary strontium chloride-choline chloride-water eutectic mixture was employed to act as both synthesis medium and template for production of the SrF_2 nanoparticles. Because of using inexpensive, safe and biocompatible precursors, low synthesis temperature, simplicity of the synthesis process, and no need of complicated laboratory equipment, the method developed in this study could be beneficial and further considered for large-scale synthesis. The bioactivity, biodegradability, biocompatibility and antibacterial properties of the synthesized SrF_2 nanoparticles were also investigated in this study for future potential biomedical applications.

2. Experimental

2.1. Materials

All analytical grade materials were purchased from Merck and used without additional purifications.

2.2. Preparation of deep eutectic system (DES)

Briefly, choline chloride ($C_5H_{14}ClNO$) and strontium chloride hexahydrate ($Sr(Cl)_2 \cdot 6H_2O$) were mixed in the molar ratio of 1:2, then 5 wt % deionized water was added to them. The resultant mixture was kept under vigorous stirring at 80 °C until a homogeneous and viscous solution was obtained without any solid impurities.

2.3. Synthesis of SrF2 nanoparticles

In a typical synthesis, 150 mL of as-prepared DES was poured in a flask at 80 °C on a magnetic stirrer. 2 g ammonium fluoride (NH_4F) was added to the DES and kept under stirring for 2 h (stirring speed of 700 rpm). Gradually, the clear solution became opaque followed by the formation of SrF_2 nanoparticles. After the desired time, the precipitates were separated using a centrifuge machine with centrifugation speed of 6000 rpm, washed with deionized water and re-centrifuged for 5 times. Finally, the precipitates were dried in a vacuum oven at 60 °C for 12 h.

2.4. Characterization of SrF2 nanoparticles

Siemens D-500 X-ray diffractometer (XRD) with CuKα radiation (λ = 1.5406 Å) was employed to study the crystalline structure of the synthesized nanoparticles. The analysis was performed at the diffraction angle of 2θ = 20–80° with a scan speed of 2°min^{-1} and step size of 0.02°. Debye-Scherrer equation was used to calculate the mean diameter of SrF_2 crystals based on the broadening of diffractions [16]:

$$D_{hkl} = \frac{K \times \lambda}{\beta \times \cos\theta} \tag{1}$$

where, λ is the wavelength of the X-rays, which is equivalent to 0.15406 nm, θ is the Brag's angle of diffraction, and β is the full width at half maximum (FWHM) in radian, K is the shape factor, which is chosen to be equal to 1.0 for spherical particles. Here, β is corrected as follows [17]:

$$\beta^2 = \beta_{exp}^2 - \beta_{standard}^2 \tag{2}$$

in which, β_{exp} is the measured width of the diffraction peak (experimental width) and $\beta_{standard}$ is the width due to standard sample (instrumental width).

A Tescan Mira 3 LMU field emission electron microscopy (FESEM) equipped with a Bruker Quantax 200 energy-dispersive X-ray (EDS) detector with working voltage of 2 kV was used to investigate the morphology, approximate particle size and elemental analysis of nanoparticles. To conduct the analysis, a very dilute suspension of SrF_2 nanoparticles was prepared in ethanol solvent, which was then subjected to ultrasonic waves for 20 min. A drop of the suspension was then poured onto a glass slide, which was imaged after drying and coating with gold. The average diameter of the nanoparticles was calculated from the FESEM micrographs using the SemAfore software (version 5.21).

In order to study the elemental composition of the samples, the whole FESEM image (on 1 μm scale) was selected and the EDS pattern was recorded.

A Philips CM 30 transmission electron microscope (TEM) with a working voltage of 200 kV was used to study the morphology and measure the accurate particle size of SrF_2 nanoparticles. For analysis, a dilute suspension of SrF_2 nanoparticles in ethanol was prepared, which was subjected to ultrasonic waves for 20 min. Subsequently, a drop of suspension was deposited on a carbon-coated copper grid, which was imaged after solvent evaporation.

Raman spectrometer (Senterra, Bruker) equipped with a diode laser at 785 nm was used to investigate the chemical structure of the synthesized nanoparticles.

2.5. Weight loss percentage

The test was performed in the artificial saliva (AS) solution prepared according to the instruction described by Fusayama et al. [18]. The pH of the solution was 5.5. The nanopowders were soaked in AS solution at ratio of 10 mg/mL in an incubator shaker at 170 rpm and 37 °C. The initial amount of the powders was 150 mg. The solution was changed every two days. When sampling, the soaked nanoparticles were washed

with deionized water and acetone and finally dried in an oven at 50 °C. The weight loss of SrF_2 nanoparticles soaked in the AS solution was calculated according to the following equation [19]:

$$\%\text{Weight loss} = \frac{W_0 - W_t}{W_0} \times 100 \qquad (3)$$

in which, W_0 is the initial weight of the nanoparticles and W_t is the weight after immersion in the AS solution.

The Metrohm 827 pH Lab was used to record changes in the pH of AS solution. The concentration of released Sr^{2+} ions into the solution was measured by an Optima 8000 inductively coupled plasma-optical emission spectrometry (ICP-OES) spectrometer. To measure the concentration of the released F^- ion, a Fluoride-ISE Metrohm fluoride selective electrode was used.

The kinetics of ion release from SrF_2 nanoparticles into the AS solution was described by Korsmeyer-Peppas model, which is expressed as the following formula [20]:

$$\frac{M_t}{M_\infty} = kt^n \qquad (4)$$

in which, M_t/M_∞ is the fraction of the released ion at time t, k is the rate constant, and n is the release exponent.

2.6. Bioactivity test

The test was performed in the simulated body (SBF) prepared according to Kokubo's recipe declared in Ref. [21]. For testing, the nanopowders and SBF were mixed in a 10 mg/mL ratio and the resulting mixture was placed in an incubator shaker at 170 rpm and 37 °C. The SBF solution was renewed every two days. When sampling, the powder was washed with deionized water and acetone and dried in an oven at 50 °C. The formation of bioactive apatite on the surface of the nanoparticles was studied by Raman spectrometer (Senterra, Bruker) equipped with a diode laser at 785 nm and SEM-EDS (AIS2300C, Seron Technologies).

2.7. Antibacterial properties of nanoparticles

Firstly, the bacterium (*Streptococcus mutans* IBRC-M 10682) was cultured in a Brain Heart Infusion medium and incubated at 37 °C. A suspension of bacteria in contact with the sterilized nanoparticles was prepared and incubated at 37 °C and 160 rpm for 24 h. Afterwards, 0.5 mL of the suspension was picked up and was added to 4.5 mL of the physiological saline containing 0.4% sodium chloride (pH 7.4) in a flask tube. The diluted bacterial suspensions of 10^{-1}, 10^{-2}, 10^{-3}, 10^{-4}, 10^{-5} and 10^{-6} were prepared and the optimal values of 25, 50, 75 and 100 μl of each suspension was transferred to petri dishes to determine the optimum dilution for colony counting. After incubation at 37 °C for 24 h, colonies were counted by Sana SL-902 colony counter and compared with the control sample. The percent reduction of colony (R%)

was calculated as follows:

$$R(\%) = \frac{(A - B)}{A} \times 100 \qquad (5)$$

where, A is the number of counted viable bacteria (CFU/mL) in control sample, and B is the number of counted viable bacteria (CFU/mL) in the presence of SrF_2 nanoparticles.

2.8. MTT cytotoxicity assay

The cytotoxicity of as-synthesized SrF_2 nanoparticles was assessed by colorimetric MTT (3-(4,5-dimethylthiazol-2-yl)-2,5-diphenyltetrazolium bromide) tetrazolium reduction assay. The human mesenchymal stem cells (hMSCs) were cultured in 75 mL flasks using 12 mL of culture medium with high glucose content (DMEM-h, Gibco, Germany) along with 5.0 wt% of fetal bovine serum (FBS, Gibco, Germany) and 1 wt% of antibiotic (Penicillin-Streptomycin, Gibco, Germany). The flasks were incubated under 90% RH, 5% CO_2 and 37 °C. The culture medium was renewed every two days as long as the cell density reaches ≥ 90%. After passaging, the hMSCs were removed from the bottom of the flask using 0.2% solution of triypsin-EDTA (Gibco, Germany) and finally counted using a Neubauer chamber.

The hMSCs were seeded in a 96-well microplate (cell density of 1×10^4 cells per well) loaded by 100 μg SrF_2 nanoparticles, which were already sterilized by ethanol (70 wt%), UV radiation for 20 min and autoclaving at 120 °C for 30 min. The supernatant was removed and an amount of 200 μl of culture medium containing 20 μl of MTT solution (Sigma Aldrich, USA) was added to the wells, which then were incubated at 37 °C, 98% RH, and 5% CO_2 for 4 h. The supernatant was removed again and 100 μl of dimethyl sulfoxide (DMSO, Sigma Aldrich) was added to dissolve the Formosan crystals. The optical absorbance of the resulted blue-violet solution was measured by ELISA microplate reader (Sunrise-Tecan, Austria) at $\lambda = 570$ nm.

2.9. Cell viability test

The viability of hMSCs in presence of as-synthesized SrF_2 nanoparticles was examined using acridine orange (AO) staining test. To this end, the dual fluorescent staining solution (1 μl) containing 100 μg/mL AO (Sigma Aldrich, USA) was added to the cell culture wells which were subsequently washed by PBS. The wells then were monitored by fluorescent microscope (Leica 090–135002, Germany) for cell viability assessment.

3. Results and discussion

The XRD pattern of the SrF_2 nanoparticles is shown in Fig. 1. From the figure, the diffraction peaks at 2θ = 26.35, 30.61, 44.11, 52.14, 54.71, 64.20, 70.76 and 72.85° characterized by crystallographic planes of (111), (200), (220), (311), (222), (400), (331) and (420) are indexed
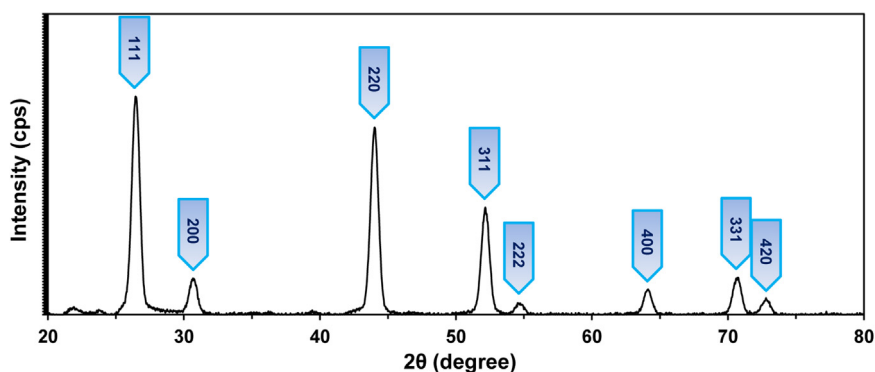
Fig. 1. XRD pattern of as-synthesized SrF_2 nanoparticles.
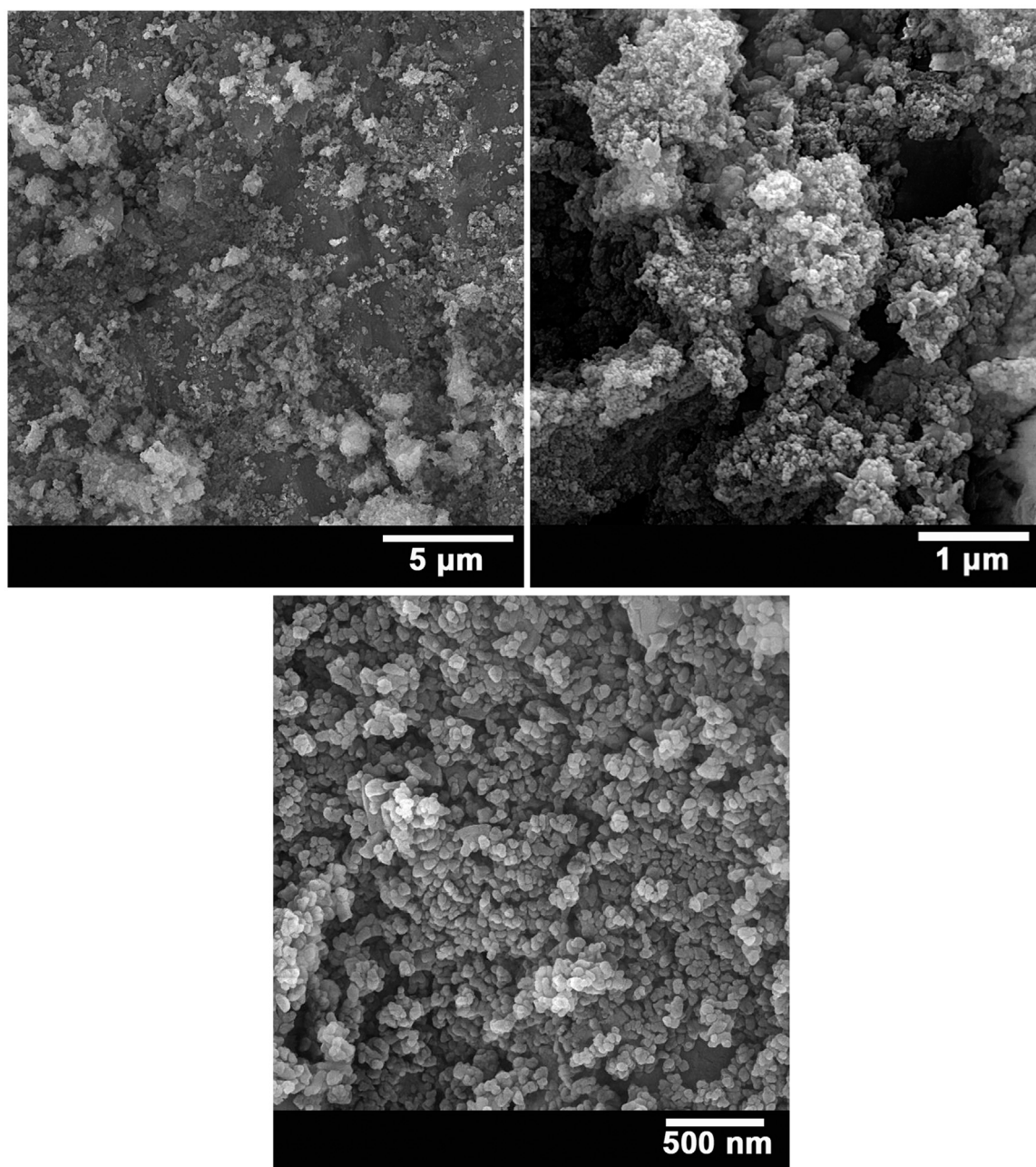
Fig. 2. FESEM micrographs of SrF_2 nanoparticles in different magnifications.

to the reference code JCPDS No. 01-086-2418 assigning to the strontium fluoride crystallized in the cubic crystal system with the space group *Fm*-3*m* and lattice constants a = b = c = 5.7940 Å. The pattern represents the broad diffractions characteristic of nanocrystalline materials. There is no diffraction due to other crystalline structures (impurities) suggesting the reasonable phase purity of the synthesized SrF_2 nanoparticles [22,23].

From the broadening of the peak with relative intensity of 100%, i.e., peak (111), the mean diameter of SrF_2 crystals is calculated to be ~ 26 nm.

FESEM micrographs of the synthesized SrF_2 nanoparticles are shown in Fig. 2. The figure clearly shows the formation of nanoscale particles with spherical morphology and particle size ranged from 30 to 50 nm. The agglomeration observed in the micrographs can be attributed to both the intrinsic tendency of nanoparticles to be agglomerated and the quality of sample preparation for FESEM analysis.

Fig. 3 shows the TEM micrograph of the SrF_2 nanoparticles. In confirmation of the FESEM observation, the TEM image also shows the formation of nanoscale particles with an average size of 40 nm.

The EDS pattern of the as-synthesized SrF_2 nanoparticles is shown in Fig. 4. The characteristic peaks of two constituent elements of SrF_2, i.e., strontium (Sr) and fluorine (F), are seen in the pattern. The absence of peaks associated with other elemental impurities in the pattern suggests the reasonable elemental purity of as-synthesized nanoparticles. Based on the semi-quantitative data obtained from EDS pattern, the Sr/F atomic ratio in as-synthesized nanoparticles is calculated to be 1.85, which is close to the stoichiometric ratio in empirical formula of SrF_2.

Fig. 5 shows the Raman spectrum of SrF_2 nanoparticles. The spectrum only demonstrate a strong band located at 285 cm^{-1}, which is due to the first order Raman scattering F_{2g} mode in SrF_2 structure. SrF_2 shows cubic symmetry with space group of O_h^5. Two nonequivalent fluorine atoms as well as the strontium cation lie on face centered cubic
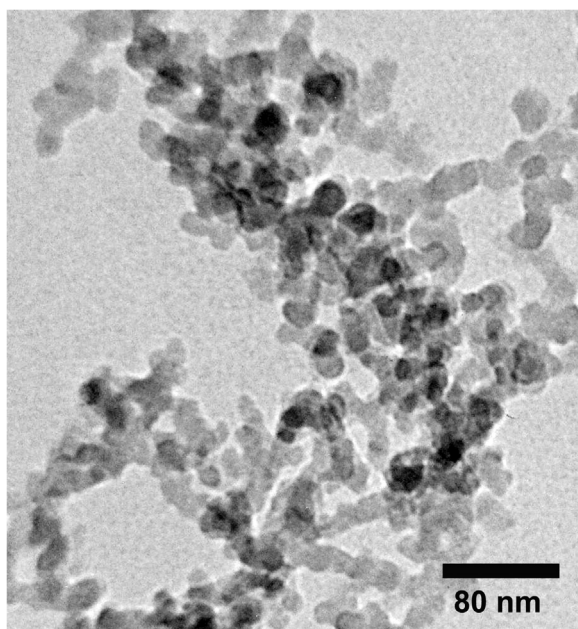
Fig. 3. TEM micrograph of the synthesized SrF$_2$ nanoparticles.
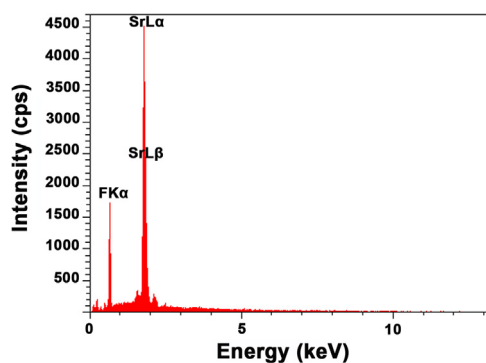
Fig. 4. EDS pattern of as-synthesized SrF$_2$ nanoparticles.
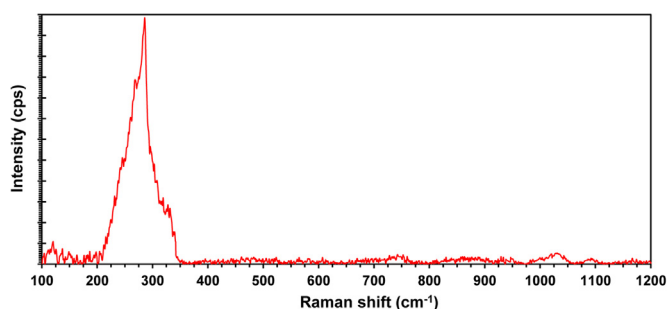
Fig. 5. Raman spectrum of the synthesized SrF$_2$ nanoparticles.

lattices. The triply degenerate F$_{2g}$ mode is a Raman active mode and appears as a strong band at $\sim 283\,\mathrm{cm}^{-1}$ [24,25].

Here, the eutectic system resembles a comprehensive synthesis system, which acts as a solvent, reactant (due to the presence of strontium in its molecular structure) and a particle growth controller (template). Owing to its high ionic strength (ionic density), the DES provides a kind of electrostatic stability to control the particle growth and prevent agglomeration. In addition, the macromolecular structure and bulky geometry of the DES can provide the necessary spatial inhibition to prevent the formation of larger particles through particle surrounding and surface adsorption on the surface of the particles.

Thus, the eutectic system can provide both electrostatic stability and spatial stability, i.e., the required electrosteric stability to control the growth of particles in nanoscale [26–29].

To determine the *in vitro* degradation of the synthesized SrF$_2$ nanoparticles, the variation of weight, pH fluctuations and release of strontium and fluorine ions were studied in the AS solution.

Fig. 6(a) shows the trend of SrF$_2$ weight variations upon immersion in the AS over a period of 14 days. The graph shows an increasing weight loss during the early days of immersion. Over the time, the degradation is gradually reduced until it reaches a relatively stable level. The plot of pH fluctuations and release profiles of Sr^{2+} and F$^-$ ions respectively shown in Fig. 6(b)–(d), demonstrate the trends in agreement with the variation trend of weight loss. The significant increase in pH and weight loss during the first days of immersion can be attributed to the higher release of strontium and fluoride ions especially alkaline Sr^{2+} ions.

Significant solubility and increased-ion release of the synthesized SrF$_2$ powders can be attributed to their nanoscale size and high specific surface area. Recent theoretical and experimental studies clearly show that the decreased particle size to nanoscale contributes to the increased dissolution and saturation solubility. The effect of particle size on solubility can be related to that on dissolution thermodynamic properties. Based on thermodynamic studies, the particle size remarkably affected the dissolution thermodynamic properties and the equilibrium constant. Upon decrease of the particle size to nanometer range, the dissolution equilibrium constant increases, while the standard dissolution Gibbs free energy, the standard dissolution enthalpy and the standard dissolution entropy decrease. Due to the linear relation between the reciprocal of particle size and the logarithm of the dissolution equilibrium constant, the standard dissolution Gibbs free energy, the standard dissolution enthalpy and the standard dissolution entropy, it is expected that the particle size strongly alter the dissolution [30,31].

The plot of Log(M_t/M_∞) *vs.* Log$t$ for release of Sr^{2+} and F$^-$ ions from SrF$_2$ nanoparticles into the AS solution is shown in Fig. 7.

The obtained values for n is used to discuss about the release mechanism. Accordingly:

  I. If $n \leq 0.45$, the release is controlled by Fickian diffusion,
 II. If $0.45 < n < 0.89$, the release is controlled by non-Fickian diffusion,
III. If n = 0.89, the release is controlled by Case-II transport,
IV. If n > 0.89, the release is controlled by Supper Case-II transport [32].

In Table 1, the calculated values of n and k for ion release from SrF$_2$ nanoparticles are presented. Based on the values obtained for n, one can claim that the release of ions (whether F$^-$ or Sr^{2+}) from SrF$_2$ nanoparticles follows Fickian diffusion mechanism and the rate of ion release is a function of $t^{-0.5}$. In addition, the obtained k values indicate the higher release rate of Sr^{2+} compared to F$^-$.

SEM micrographs obtained on the surface of SrF$_2$ nanoparticles after 14 days of immersion in the SBF are shown in Fig. 8. The images represent the formation of densified cauliflower-like nanostructures on the surface of nanoparticles, which are characteristic of nanocrystalline biological apatite. The bioactive apatite nanostructures covers the whole surface of the SrF$_2$ nanoparticles after 14 days showing the good *in vitro* bioactivity of nanoparticles [33].

The EDS pattern of SrF$_2$ nanoparticles after 14 days of soaking in the SBF is shown in Fig. 9. The pattern represents the dominant peaks related to calcium and phosphorus, which can be attributed to the formation of bioactive apatite layer on the surface of SrF$_2$ nanoparticles. Since the EDS analysis is a kind of surface analysis with low intrusive depth and, given the formation of densified apatite layer on the surface of the nanoparticles (as inferred from the SEM micrographs), it is evident that the EDS peaks related to the calcium and phosphorus in the
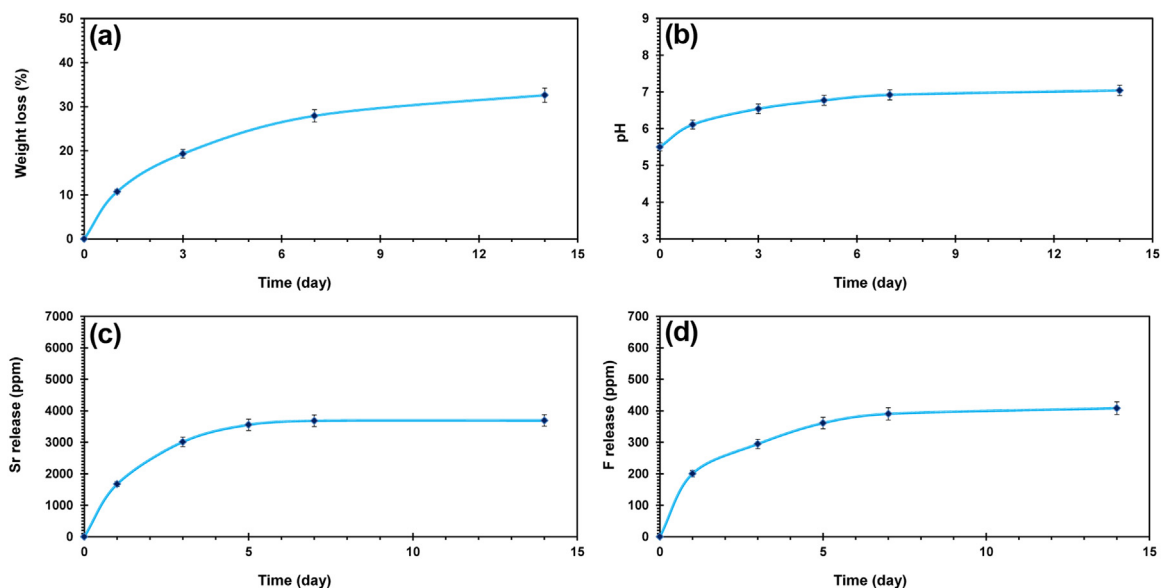
Fig. 6. (a) Weight loss plot, (b) plot of pH variations, (c) release profile of Sr^{2+} ion and (d) release profile of F^- ion during the immersion of SrF_2 nanoparticles in the AS solution.
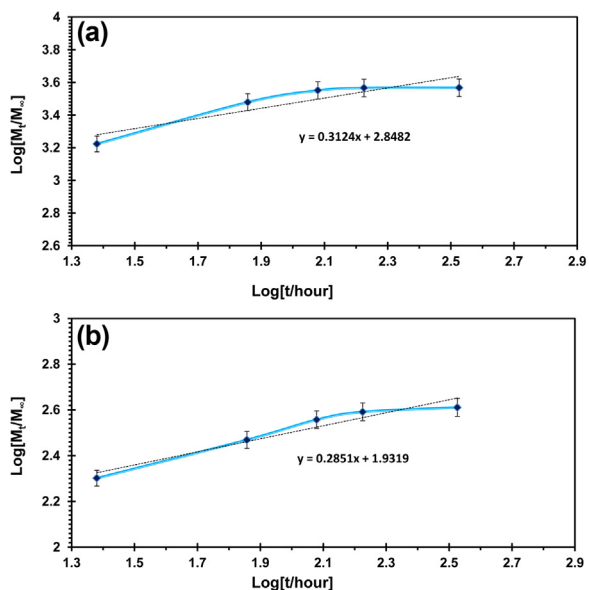
Fig. 7. The plot of $Log(M_t/M_\infty)$ against Logt for of (a) Sr^{2+} and (b) F^- ions released from SrF_2 nanoparticles into the AS solution.

Table 1
Calculated values of n and k for release of Sr^{2+} and F^- ions from SrF_2 nanoparticles into the AS solution.

Sample (release environment)	F^- release		Sr^{2+} release	
	n	*k*	*n*	*k*
SrF_2 nanoparticles (AS)	2.85×10^{-2}	$0.85 \times 10^{+2}$	3.12×10^{-2}	$7.05 \times 10^{+2}$

biological apatite are prominent than fluorine and strontium in the SrF_2.

The Raman spectrum of SrF_2 nanoparticles after 14 days of immersion in the SBF is shown in Fig. 10. The dominant peak at 963 cm^{-1} is attributed to the hydroxyapatite (965 cm^{-1}) or the fluorapatite (960 cm^{-1}). Owing to release of fluoride from SrF_2 nanoparticles, it seems that the bioactive apatite formed on the surface of the
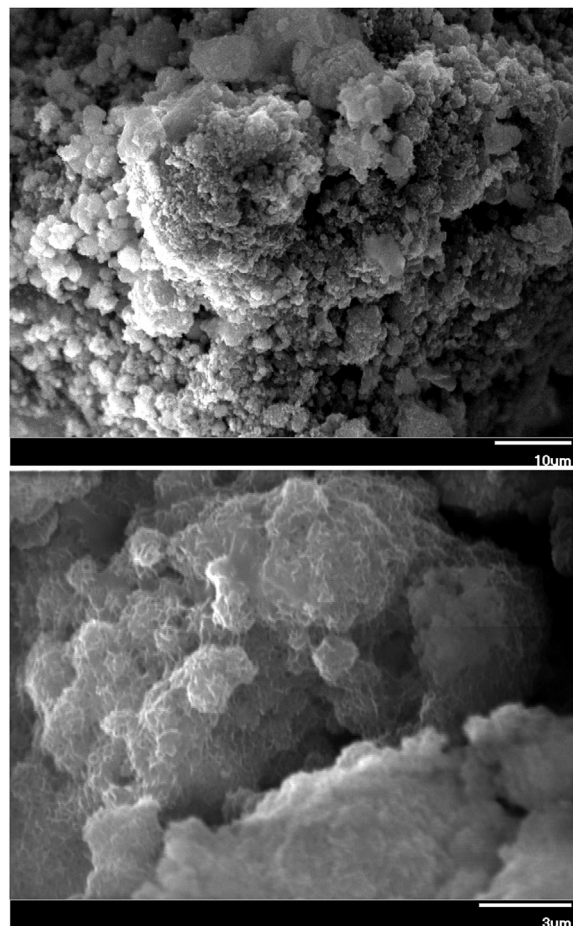
Fig. 8. SEM micrographs from the surface of SrF_2 nanoparticles after 14 days of immersion in the SBF.

nanoparticles also contains fluorine; in other words, a combination of hydroxyapatite and fluorapatite, i.e., fluor-hydroxyapatite, is formed on the surface of nanoparticles. Since fluoride ion (F^-) is smaller in size than hydroxyl ion (OH^-), the substitution of OH^- by F^- in apatite results
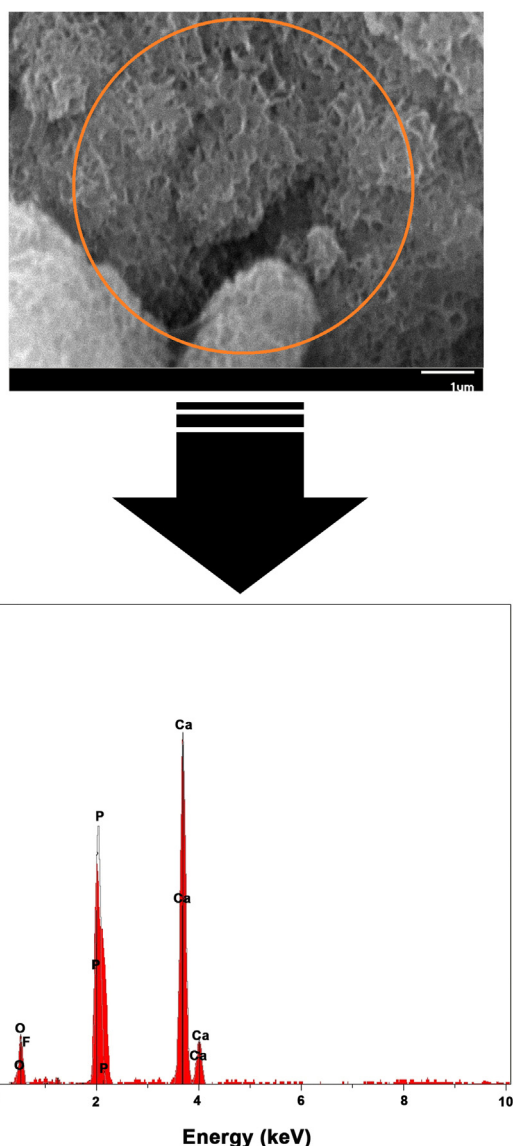
Fig. 9. EDS pattern recorded on the surface of SrF$_2$ nanoparticles after 14 days in the SBF.
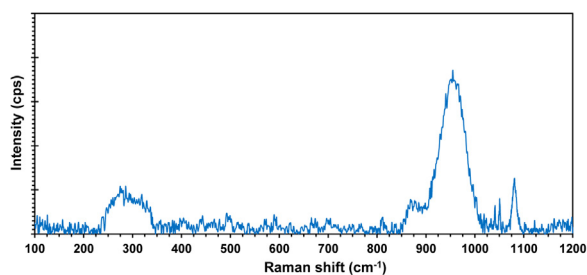
Fig. 10. Raman spectrum of SrF$_2$ nanoparticles after immersion in the SBF for 14 days.

in a structural contraction or a volume reduction of about 1%. The direct consequence of the structural contraction is decrease of the lattice constants in apatite. This is associated with some variations in the vibrational modes of the phosphate group (PO_4^{3-}) as the only active vibration modes in Raman spectroscopy, which is detectable by displacement of the vibrational mode of phosphate group by 5 cm^{-1}.

Regarding the formation of densified bioactive apatite nanostructures on the surface of SrF$_2$ nanoparticles, and according to the

depth of penetration and identification in Raman analysis, the peak related to the base material, i.e., strontium fluoride, located at 285 cm^{-1}, shows lower intensity than that of apatite. Another peak at about 1080 cm^{-1} appeared as a result of immersion in the SBF, is attributed to carbonate groups (CO_3^{2-}) in the calcite structure. Overall, Raman analysis confirms the formation of bioactive carbonated-fluorhydroxyapatite on the surface of SrF$_2$ nanoparticles upon immersion in the SBF for 14 days [34–36].

The aforementioned changes on SrF$_2$ nanoparticles upon immersion in the SBF medium that lead to the formation of bioactive carbonated-fluorhydroxyapatite can be explained as follows: Initially, a fast ion exchange occurs between Sr^{2+} and H$^+$ or H$_3$O$^+$ ions in the solution. This step is controlled by the diffusion process, which causes hydrolysis and the formation of hydroxyl groups such as –Sr–OH on the surface of SrF$_2$ nanoparticles. During such a process, the solution pH increases as a result of ion exchange between H$_3$O$^+$ ions in the solution and alkaline Sr^{2+} ions released from SrF$_2$ nanoparticles. The as-formed hydroxyl groups on the surface of SrF$_2$ nanoparticles act as active sites for germination and formation of bioactive apatite nucleus. In this way, the calcium and phosphate ions in the SBF migrate to the surface of the nanoparticles and form a rich layer of CaO-P$_2$O$_5$ on the surface. The as-formed amorphous CaO-P$_2$O$_5$ layer gradually grows and crystallizes with further inclusion of calcium and phosphate ions. Finally, due to the crystallization of the amorphous CaO-P$_2$O5 layer, the crystalline bioactive apatite layer with inclusion of OH$^-$, CO$_3^{2-}$ and F$^-$ (released from SrF$_2$ into the solution) anions is formed on the surface of SrF$_2$ nanoparticles [37].

Antibacterial efficiency of as-synthesized SrF$_2$ nanoparticles was assessed against the bacterial strain of *Streptococcus mutans*. Fig. 11 shows the bacteria culture media in the absence (control sample) and presence of SrF$_2$ nanoparticles. The figure clearly shows that the
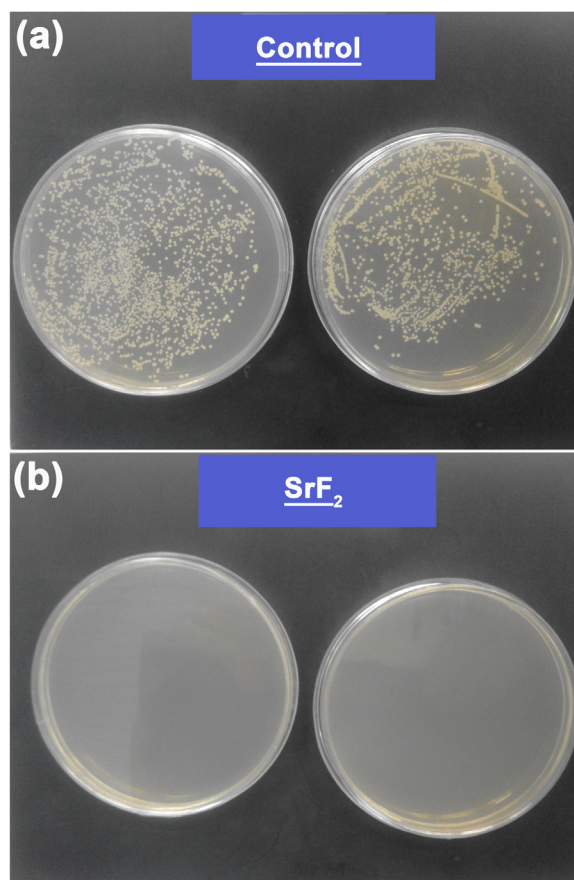
Fig. 11. The images of the bacteria culture medium in the (a) absence (control sample) and (b) presence of SrF$_2$ nanoparticles.

bacteria are almost eliminated in contact with SrF$_2$ nanoparticles suggesting the excellent antibacterial property.

According to the obtained data on the percent reduction of colony (R%), SrF$_2$ nanoparticles cause the colony reduction close to 100% showing the maximum antibacterial activity against *Streptococcus mutans* bacterium. The high antibacterial activity of the synthesized SrF$_2$ nanoparticles could be attributed to the sustained release of ions, especially fluoride.

Based on the results of recent studies, fluoride can affect the metabolism of bacteria in a number of ways with completely different mechanisms. Based on a mechanism, fluoride can directly act as inhibitor for an enzyme like glycolytic enzyme enolase or directly attached to heme-based peroxidases. The flavin-based peroxidases of many oral bacteria are insensitive to fluoride. Therefore, as another possible mechanism, fluoride can form metal-complexes such as AlF$_4^-$, which is the major inhibitor of proton-translocating F-ATPases. F-ATPases can mimic the phosphate group of ATP to form an abortive complex with ADP at the active, hydrolytic sites of the enzymes. This same kind of inhibition has been found in the case of *Streptococcus mutans* and *Lactobacillus casei*. However, the actions of fluoride, which is known for its anti-decay properties, are those resulted from its weak-acid property. Fluoride increases the permeability of the bacterial membrane to the protons and compromises the functioning of the F-ATPases in exporting protons, thereby inducing cytoplasmic acidification and acid inhibition of glycolytic enzymes. In fact, fluoride reduces the acid tolerance of bacteria under acidic conditions of cariogenic plaque, which causes complete arrest of glycolysis by intact cells of *Streptococcus mutans*. Antibacterial properties of fluoride appears to be mainly due to its weak-acid character [7,38–40].

Fig. 12(a) shows the optical density (OD) of hMSCs cultivated on the SrF$_2$ nanoparticles as examined by MTT assay during 7 days. Based on the obtained data, there is no significant cells (p > 0.05) between OD values of hMSCs in the absence (control sample) and presence of SrF$_2$ nanoparticles over the studied time period. Therefore, it can be deduced that SrF2 nanoparticles shows no cytotoxic effect on hMSCs. Fig. 12(b) and (c) shows the fluorescence micrographs of the stained hMSCs with acridine orange (AO). As a confirmation of MTT results, AO staining test clearly shows that the SrF$_2$ nanoparticles not only does not endanger the cellular life, but also improves it to a desired level, which is inferred from the unchanged cell shape and increased density of the green zones in the image. It should be remembered that the living and dead cells are respectively visible in green and red under the fluorescent microscope after AO staining. Although some studies point to toxic effects of fluoride on the cells, but no harmful effect have been observed here, which can be attributed to the sustained release of fluoride from SrF$_2$ nanoparticles [4,33]. The results obtained on MTT assay and AO staining test endorse the non-cytotoxicity and biocompatibility of as-synthesized SrF$_2$ nanoparticles.

4. Conclusion

The ternary deep eutectic system (DES) based on choline chloride-strontium chloride-water was successfully employed for synthesis of strontium fluoride (SrF$_2$) nanoparticles. The characterization results approved the synthesis of SrF$_2$ particles with a cubic crystal structure, mean crystal diameter of 26 nm, average particle size of 40 nm, Sr/F atomic ratio of 1.85 and reasonable elemental and structural purity. In accordance with the suggested synthesis mechanism, the DES simultaneously acts as solvent (due to the fluid nature of the system at ambient temperature), reacting agent (due to having strontium in the molecular structure), and template (due to the high ionic strength and macromolecular geometry providing more control over particle formation and growth). The bioactivity test in the SBF showed the formation of bioactive carbonated-fluorhydroxyapatite nanostructures on the surface
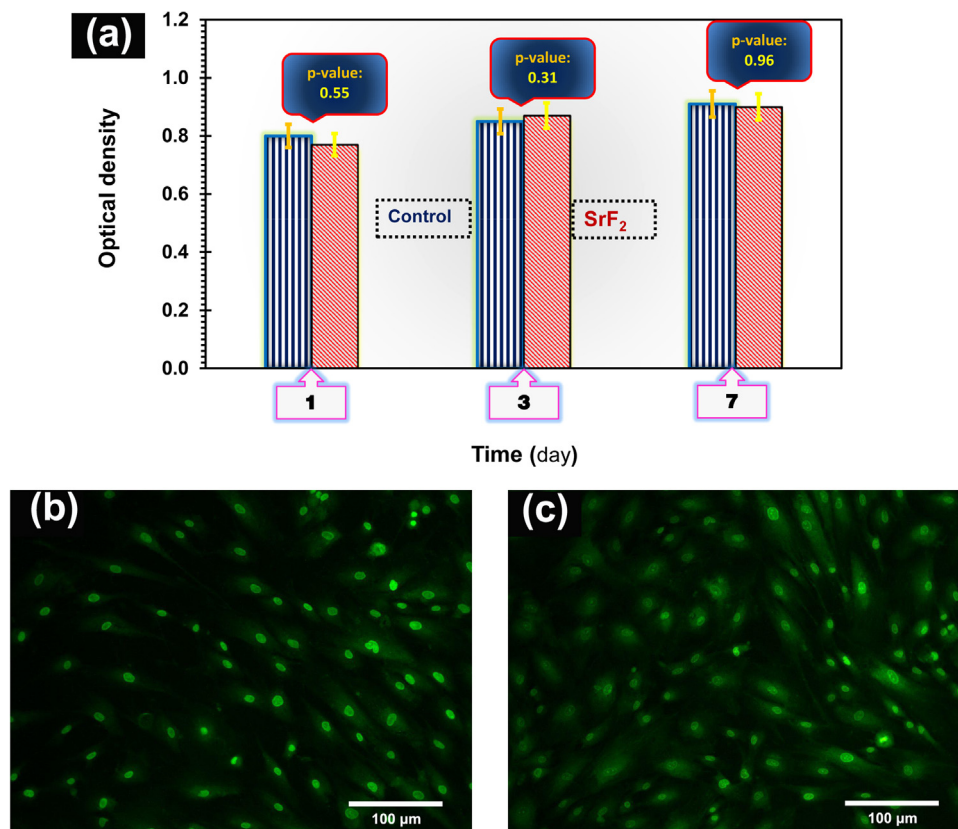
Fig. 12. (a) The optical density of hMSCs after culture on as-synthesized SrF$_2$ nanoparticles; fluorescence micrographs of hMSCs stained with AO after 7 days in the (b) absence (control) and (c) presence of SrF$_2$ nanoparticles.

SrF_2 nanoparticles as confirmed by SEM-EDS and Raman spectroscopy. Antibacterial study on *Streptococcus mutans* showed the 100% antibacterial efficiency of as-synthesized SrF_2 nanoparticles induced by increased pH and osmotic pressure of the environment due to the boosted Sr^{2+} and F^- ion release from the synthesized nanoparticles with high surface area and reactivity. MTT cytotoxicity assay and acridine orange staining test on hMSCs confirmed the non-cytotoxicity and biocompatibility of SrF_2 nanoparticles.

We believe that the present study could be of importance because of providing a green and facile method for the synthesis of biocompatible SrF_2 nanostructures with good antibacterial and bioactivity properties demanded for biomedical applications.

Acknowledgement

References

[1] M. Azami, S. Jalilifiroozinezhad, M. Mozafari, M. Rabiee, Synthesis and solubility of calcium fluoride/hydroxy-fluorapatite nanocrystals for dental applications, Ceram. Int. 37 (2011) 2007–2014.

[2] J. Liu, S.C.F. Rawlinson, R.G. Hill, F. Fortune, Fluoride incorporation in high phosphate containing bioactive glasses and in vitroosteogenic, angiogenic and antibacterial effects, Dent. Mater. 32 (2016) e221–e237.

[3] P. Kosior, M. Dobrzyński, M. Korczyński, K. Herman, A. Czajczyńska-Waszkiewicz, M. Kowalczyk-Zając, D. Piesiak-Pańczyszyn, K. Fita, M. Janeczek, Long-term release of fluoride from fissure sealants–In vitro study, J. Trace Elem. Med. Biol. 41 (2017) 107–110.

[4] W.A. Bala, V.S. Benitha, K. Jeyasubramanian, G.S. Hikku, P. Sankar, S. Vignesh Kumar, Investigation of anti-bacterial activity and cytotoxicity of calcium fluoride nanoparticles, J. Fluor. Chem. 193 (2017) 38–44.

[5] A. Wiegand, W. Buchalla, T. Attin, Review on fluoride-releasing restorative materials-Fluoride release and uptake characteristics, antibacterial activity and influence on caries formation, Dent. Mater. 23 (2007) 343–362.

[6] H.O. Simila, N. Karpukhina, R.G. Hill, Bioactivity and fluoride release of strontium and fluoride modified Biodentine®, Dent. Mater. 34 (2018) e1–e7.

[7] R.E. Marquis, Antimicrobial actions of fluoride for oral bacteria, Can. J. Microbiol. 41 (1995) 955–964.

[8] J.M. ten Cate, C. van Loveren, Fluoride mechanisms, Dent. Clin. N. Am. 43 (1999) 713–742.

[9] H.H.K. Xu, J.L. Moreau, L. Sun, L.C. Chow, Strength and fluoride release characteristics of a calcium fluoride based dental nanocomposite, Biomaterials 29 (2008) 4261–4267.

[10] P.P. Fedorov, A.A. Luginina, S.V. Kuznetsov, V.V. Osiko, Nanofluorides, J. Fluor. Chem. 132 (2011) 1012–1039.

[11] P.T. Anastas, J.C. Warner, Green Chemistry: Theory and Practice, Oxford University Press, Oxford, UK, 1998.

[12] A. Lashgari, S. Ghamami, M. Golzani, G. Salgado-Morán, D. Glossman-Mitnik, L. Gerli-Candia, B. Abdolmaleki, Preparation, identification and biological properties of new fluoride nanocompounds, J. Chil. Chem. Soc. 61 (2016) 3201–3205.

[13] Y.P. Du, X. Sun, Y.W. Zhang, Z.G. Yan, L.D. Sun, C.H. Yan, Uniform alkaline earth fluoride nanocrystals with diverse shapes grown from thermolysis of metal trifluoroacetates in hot surfactant solutions, Cryst. Growth Des. 9 (2009) 2013–2019.

[14] L. Schmidt, F. Emmerling, H. Kirmse, E. Kemnitz, Sol–gel synthesis and characterisation of nanoscopic strontium fluoride, RSC Adv. 4 (2014) 32–38.

[15] R.N. Grass, W.J. Stark, Flame synthesis of calcium-, strontium-, barium fluoride nanoparticles and sodium chloride, Chem. Commun. 0 (2005) 1767–1769.

[16] B.D. Cullity, Elements of X-ray Diffraction, Addison-Wesley publishing, Boston, USA, 1977.

[17] M. Karimi, S. Hesaraki, M. Alizadeh, A. Kazemzadeh, Synthesis of calcium phosphate nanoparticles in deep-eutectic choline chloride-urea medium: investigating the role of synthesis temperature on phase characteristics and physical properties, Ceram. Int. 42 (2016) 2780–2788.

[18] I. Mutlu, E. Oktay, Characterization of 17-4 PH stainless steel foam for biomedical applications in simulated body fluid and artificial saliva environments, Mater. Sci. Eng. C 33 (2013) 1125–1131.

[19] M. Barbeck, T. Serra, P. Booms, S. Stojanovic, S. Najman, E. Engel, R. Sader, C. James Kirkpatrick, M. Navarro, S. Ghanaati, Analysis of the in vitro degradation and the in vivo tissue response to bi-layered 3D-printed scaffolds combining PLA and biphasic PLA/bioglass components–guidance of the inflammatory response as basis for osteochondral regeneration, Bioact. Mater. 2 (2017) 208–223.

[20] G. Singhvi, M. Singh, In-vitro drug release characterization models, Int. J. Pharm. Stud. Res. 2 (2011) 77–84.

[21] T. Kokubo, H. Takadama, How useful is SBF in predicting in vivo bone bioactivity? Biomaterials 27 (2006) 2907–2915.

[22] M.Y.A. Yagoub, H.C. Swart, L.L. Noto, P. Bergman, E. Coetsee, Surface characterization and photoluminescence properties of Ce^{3+}, Eu co-doped SrF_2 nanophosphor, Material 8 (2015) 2361–2375.

[23] N. Kumam, N.P. Singh, L.P. Singh, S.K. Srivastava, Enhancement of luminescence in white emitting strontium fluoride core @ calcium fluoride shell nanoparticles, Nanoscale Res. Lett. 10 (2015) 374.

[24] O. Brafman, S.S. Mitra, Raman scattering by additively colored SrF_2 and BaF_2 crystals, Light Scatt. Spectra Solids 133 (1964) 543–549.

[25] S.S. Bedi, Major Singh, Jaspal Singh, Effect of temperature on the Raman frequency of fluorite solids, Solid State Commun. 89 (1994) 265–267.

[26] M. Karimi, M. Rastegar Ramsheh, S.M. Ahmadi, M.R. Madani, M. Shamsi, R. Reshadi, F. Lotfi, Reline-assisted green and facile synthesis of fluorapatite nanoparticles, Mater. Sci. Eng. C 77 (2017) 121–128.

[27] M. Karimi, S. Hesaraki, M. Alizadeh, A. Kazemzadeh, A facile and sustainable method based on deep eutectic solvents toward synthesis of amorphous calcium phosphate nanoparticles: the effect of using various solvents and precursors on physical characteristics, J. Non-Cryst. Solids 443 (2016) 59–64.

[28] M. Karimi, S. Hesaraki, M. Alizadeh, A. Kazemzadeh, Time and temperature mediated evolution of CDHA from ACP nanoparticles in deep eutectic solvents: kinetic and thermodynamic considerations, Mater. Des. 122 (2017) 1–10.

[29] M. Karimi, M. Rastegar Ramsheh, S.M. Ahmadi, M.R. Madani, One−step and low−temperature synthesis of monetite nanoparticles in an all−in−one system (reactant, solvent, and template) based on calcium chloride−choline chloride deep eutectic medium, Ceram. Int. 43 (2017) 2046–2050.

[30] Z.Q. Wang, Y.Q. Xue, Z.X. Cui, H.J. Duan, X.Y. Xia, The size dependence of dissolution thermodynamics of nanoparticles, Nano 11 (2016) 1650100.

[31] G. Kaptay, On the size and shape dependence of the solubility of nano-particles in solutions, Int. J. Pharm. 430 (2012) 253–257.

[32] R. Gouda, H. Baishya, Z. Qing, Application of mathematical models in drug release kinetics of carbidopa and levodopa ER tablets, J. Dev. Drugs 6 (2017) 171.

[33] M. Karimi, A. Jodaei, A. Sadeghinik, M. Rastegar Ramsheha, T. Mohammadi Hafshejani, M. Shamsi, F. Orandd, F. Lotfi, Deep eutectic choline chloride-calcium chloride as all-in-one system for sustainable and one-step synthesis of bioactive fluorapatite nanoparticles, J. Fluor. Chem. 204 (2017) 76–83.

[34] R. Schröder, H. Pohlit, T. Schüler, M. Panthöfer, R.E. Unger, H. Frey, W. Tremel, Transformation of vaterite nanoparticles to hydroxycarbonate apatite in a hydrogel scaffold: relevance to bone formation, J. Mater. Chem. B 3 (2015) 7079–7089.

[35] D. Bellucci, A. Sola, A. Anesi, R. Salvatori, L. Chiarini, V. Cannillo, Bioactive glass/hydroxyapatite composites: mechanical properties and biological evaluation, Mater. Sci. Eng. C 51 (2015) 196–205.

[36] M. Campillo, P.D. Lacharmoise, J.S. Reparaz, A.R. Goñi, M. Valiente, On the assessment of hydroxyapatite fluoridation by means of Raman scattering, J. Chem. Phys. 132 (2010) 244501.

[37] M. Mozafari, F. Moztarzadeh, M. Tahriri, Investigation of the physico-chemical reactivity of a mesoporous bioactive SiO_2–CaO–P_2O_5 glass in simulated body fluid, J. Non-Cryst. Solids 356 (2010) 1470–1478.

[38] E. Barboza-Silva, A.C.D. Castro, R.E. Marquis, Mechanisms of inhibition by fluoride of urease activities of cell suspensions and biofilms of *Staphylococcus epidermidis*, *Streptococcus salivarius*, *Actinomyces naeslundii* and of dental plaque, Oral Microbiol. Immunol. 20 (2005) 323–332.

[39] N. Beyth, S. Farah, A.J. Domb, E.I. Weiss, Antibacterial dental resin composites, React. Funct. Polym. 75 (2014) 81–88.

[40] L. Cheng, M.D. Weir, H.H.K. Xu, A.M. Kraigsley, N.J. Lin, S.L. Gibson, X. Zhou, Antibacterial and physical properties of calcium-phosphate and calcium-fluoride nanocomposites with chlorhexidine, Dent. Mater. 28 (2012) 573–583.